

Quantitative Analysis of Microstructures and Strength of Nb-Ti Microalloyed Steel with Different Ti Additions



XIAOLONG GAN, QING YUAN, GANG ZHAO, HONGWEI MA, WEN LIANG, ZHENGLIANG XUE, WENWEI QIAO, and GUANG XU

A quantitative analysis was carried out in the present study to determine the effects of titanium (Ti) addition on microstructures and strength of Nb-Ti microalloyed steel. The obtained results revealed that strength was significantly improved with an increase in Ti content from 0.041 to 0.079 wt pct. The difference in the yield strength between the two steel samples occurred due to the different strengthening effects of grain refinement, precipitation, and dislocation strengthening, among which the grain refinement and precipitation strengthening contributions were dominating. With a further increase in the Ti content, ferrite grains became refined. Consequently, a homogeneous ferrite microstructure was attained for high Ti contents. Moreover, large-sized (Ti, Nb)C particles manifested the Kurdjumov–Sachs (KS) relationship, whereas fine (Ti, Nb)C particles held the Baker–Nutting (BN) relationship; thus, abundant fine nanoscale (Ti, Nb)C particles formed after coiling. Furthermore, the high dislocation density facilitated the precipitation of (Ti, Nb)C particles along dislocation lines.

<https://doi.org/10.1007/s11661-020-05700-9>

© The Minerals, Metals & Materials Society and ASM International 2020

I. INTRODUCTION

THE development of microalloyed steels has been continuous for the last several decades due to their outstanding mechanical properties.^[1–5] Microalloyed steels are individually or associatedly alloyed with niobium (Nb), vanadium (V), and titanium (Ti).^[6–10] Microalloying elements usually exist in steels as solute atoms or precipitates to retard the austenite

recrystallization and the grain growth of the α phase, and the beneficial effects of Nb are generally found to be the largest as compared to other microalloying elements.^[11–14] Nanoscale carbonitride precipitates can significantly improve the strength of microalloyed steels by precipitation strengthening based on the Orowan mechanism.^[15–18] Nb precipitates are often found in the γ and α phases and easily nucleate during deformation. The lattice constant of NbC is larger than those of VN and VC; thus, NbC manifests a superior precipitation strengthening effect with the same carbide particle size and particle number density.^[19] The solubility of V in the γ phase is relatively large, thus resulting in easy precipitation inside the α phase.^[20] On the contrary, Ti-alloyed carbides nucleate and grow at a high temperature to inhibit the grain growth of the γ phase.^[21–23]

In recent years, the sustainable development strategy has become an important research area in iron and steel industries. With the development of microalloyed steels, an obvious shortcoming of high production cost (due to the high price of microalloys) in international markets has been faced; hence, a strong trend of adding more Ti during steel production has emerged due to the relatively low price of Ti ore (in comparison to Nb and V) and the excellent strength–ductility balance of Ti-microalloyed steels.^[12,15] Some studies attempted to fabricate Ti-alloyed steels or Ti-containing composite microalloyed steels for use in automobile industries. The aforementioned studies mainly focused on the dissolution

XIAOLONG GAN, GANG ZHAO, HONGWEI MA, ZHENGLIANG XUE, and GUANG XU are with The State Key Laboratory of Refractories and Metallurgy, Hubei Collaborative Innovation Center for Advanced Steels, Wuhan University of Science and Technology, Wuhan, 430081 Hubei, P.R. China and also with the Key Laboratory for Ferrous Metallurgy and Resources Utilization of Ministry of Education, Wuhan University of Science and Technology. QING YUAN is with The State Key Laboratory of Refractories and Metallurgy, Hubei Collaborative Innovation Center for Advanced Steels, and the Key Laboratory for Ferrous Metallurgy and Resources Utilization of Ministry of Education, Wuhan University of Science and Technology, and Jiangsu Huaneng Cable Company Limited, Gaoyou, 225613 Jiangsu, P.R. China. Contact e-mail: yuanqing@wust.edu.cn WEN LIANG is with The State Key Laboratory of Refractories and Metallurgy, Hubei Collaborative Innovation Center for Advanced Steels, and the Key Laboratory for Ferrous Metallurgy and Resources Utilization of Ministry of Education, Wuhan University of Science and Technology, and the Wuhan Branch of Baosteel Central Research Institute, Wuhan, 430080 Hubei, P.R. China. WENWEI QIAO is with Jiangsu Huaneng Cable Company Limited.

Manuscript submitted September 5, 2019.

Article published online March 11, 2020

behavior of second-phase particles,^[24–26] the deformation-induced ferrite transformation,^[14,27] and the microstructural and the mechanical properties of microalloyed steels.^[28–33] For instance, Yuan and Liang^[34] reported that with the addition of Ti in Nb-bearing microalloyed steels, the thermal stability of carbonitrides increased remarkably due to the formation of coarse particles. Wang *et al.*^[35] focused on the precipitation behavior of Nb and Ti and propounded that grain refinement and dislocation strengthening were the main strengthening mechanisms. Furthermore, the influences of the cooling rate before coiling on microstructural evolution, precipitates, and mechanical properties of associatedly microalloyed ferritic steels have been investigated in detail.^[36] Patra *et al.*^[37] studied the microstructure and mechanical properties of Nb-Ti-based hot-rolled steel with a yield strength of 700 MPa at different coiling temperatures. The results indicated that compared to steel coiled at 520 °C, the investigated steel, which was coiled at 580 °C, had slightly finer grains, higher dislocation density, and slightly higher precipitation of (Ti, Nb)C. However, very few studies have reported the effects of different Ti additions on Nb-Ti microalloyed steels, especially for high Ti steels. Moreover, systematically quantitative analysis of microstructures and strengths of Nb-Ti steels with low and high Ti contents has rarely been carried out. Most of the reported literature applies obscure estimation when calculating the strength contribution in experimental steels. For instance, in many works, the dislocation strengthening is often estimated to be an empirical value.^[4] In addition, the volume fraction of precipitations is artificially determined by the obtained transmission electron microscope (TEM) images of precipitation.^[12,19] Therefore, the main aim of the present study was to present a comprehensive analysis of microstructures, precipitations, and strength contribution in the Nb-Ti microalloyed steel with different Ti additions. The addition of Ti could decrease the amount of Nb or V. Furthermore, an optimal additional amount of Ti on the mechanical property of the Nb-Ti steel is crucial. Therefore, two Nb-Ti steels with different Ti additions were designed in the present work. The obtained results could provide some reference data in the design of chemical compositions of Nb-Ti steels.

II. EXPERIMENTAL PROCEDURE

The chemical compositions of two Nb-Ti microalloyed steels, namely, Nb-LTi and Nb-HTi, are presented in Table I, and their Ti contents are 0.041 wt pct (conventional addition level) and 0.079 wt pct, respectively. Further, 0.035 wt pct Nb was added to the steels because an extra addition of Nb beyond this value will have little increasing strengthening contribution.^[32] In the author's previous study,^[15] it was clarified that the strength of steels increases with the Ti content from 0.0023 to 0.108 wt pct. Two Nb-Ti steels with different Ti additions were chosen in order to quantitatively analyze the function of Ti on the microstructures and strengths of Nb-Ti steels in the present study. The

casting slab of 60-mm thickness (produced by thin slab casting and rolling) was reheated to 1230 °C and held for 35 minutes in a soaking furnace. Then, the continuous casting slab was hot rolled into 2-mm-thick strips through seven pass rollings on a continuous hot-strip mill. The starting and the finishing rolling temperatures were set to 1080 °C and 880 °C, respectively. Finally, the strips were laminar cooled with an estimated cooling rate of 75 °C/s to 630 °C after rolling and then coiled, followed by air cooling from the coiling temperature to room temperature. The total length of the coil strip was 700 to 800 m.

Samples were taken from 2-mm-thick strips. Standard tensile specimens were machined along the rolling direction of the strip and tested on an Instron 5900 universal tensile testing machine at room temperature. Duplicate tests were carried out to ensure the accuracy of the experiments. The hardness measurement along the thickness direction was also conducted on an HV-1000 hardness testing machine under a loading force of 100 g and a loading time of 10 seconds to evaluate the microstructural homogeneity in the samples. A thickness interval of 0.5 mm was used from the top surface to the bottom surface along the thickness direction of the specimens, and an average value of six points in the same level was used as the measured hardness. The microstructural evaluation was performed on a field-emission-scanning electron microscope (FE-SEM) with an accelerating voltage of 20 kV. The electron backscatter diffraction (EBSD) technique was employed for crystallographic characterization, and grain sizes were measured. Moreover, the kernel average misorientation (θ) was determined from the EBSD data. The EBSD specimens were electropolished at a voltage of 40 mV in an electrolyte consisting of 10 vol pct perchloric acid and 90 vol pct glacial acetic acid; a step size of 0.2 μm was applied to obtain high-quality images. Carbon replica and thin foils were prepared to observe and analyze the microstructures of carbides on a JEM-2100F TEM (equipped with energy-dispersive spectroscopy (INCA-EDS)) at 200 kV. In addition, a Zeiss Auriga focused ion beam-scanning electron microscope (FIB-SEM) was used to observe large-sized TiN particles, and their chemical components were analyzed by EDS.

III. RESULTS AND DISCUSSION

A. Mechanical Properties

The strength and Vickers hardness of the tested steels are presented in Figure 1. The tensile and the yield strengths of Nb-LTi steel were, respectively, measured as 664 and 611 MPa, which were significantly lower than those of Nb-HTi steel (775 and 714 MPa, respectively); therefore, the difference in yield strength between these two steels was 103 MPa. Figure 2 gives one group of the stress-strain curves of the Nb-HTi and Nb-LTi steels. It is clear that the total elongations for the two steels both closed to 20 pct, in which the Nb-LTi steel had a relatively better ductility. Strain hardening was found in

Table I. Chemical Compositions of Nb-Ti Microalloyed Steels (Weight Percent)

Steel	C	Si	Mn	Cr	N	Nb	Ti	P	S	Al
Nb-LTi	0.054	0.115	1.173	0.200	0.0035	0.033	0.041	0.012	0.004	0.033
Nb-HTi	0.052	0.117	1.171	0.202	0.0041	0.034	0.079	0.015	0.003	0.030

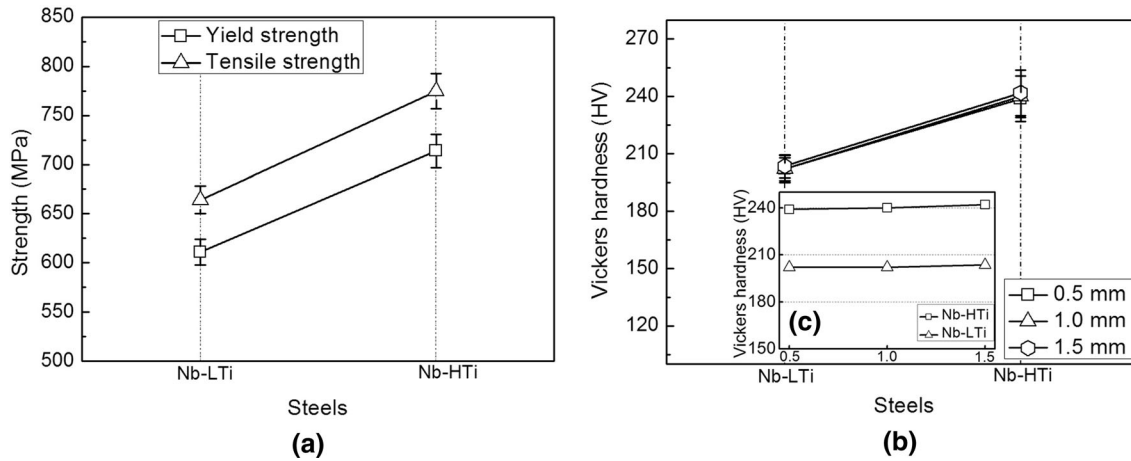


Fig. 1—(a) Strengths and (b) Vickers hardnesses of Nb-HTi and Nb-LTi steels and (c) Vickers hardness along the thickness of steels.

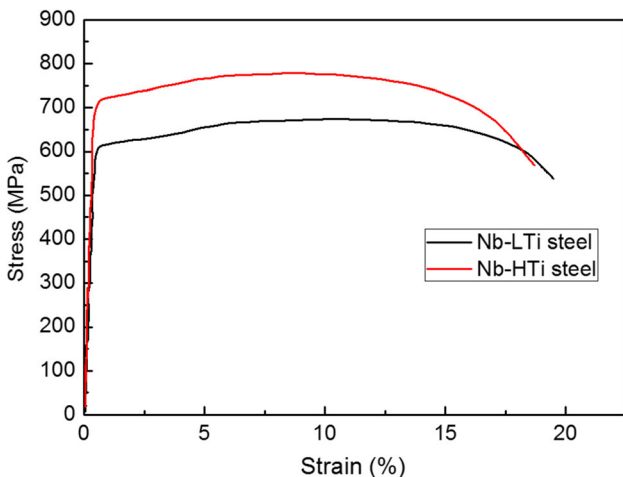


Fig. 2—Stress-strain curves of the Nb-HTi and Nb-LTi steels.

the curves after yielding and the stress apparently decreased after necking. Similarly, the average hardness in the 1/4-thickness position of Nb-LTi steel was measured as 201 HV, which is much smaller than that of Nb-HTi steel (239 HV). No apparent variation in hardness was noticed along the thickness direction (Figure 1(c)), thus revealing the presence of homogeneous microstructures in the specimens. The temperature gradient along the thickness direction of the strips was eliminated in 3 seconds by laminar cooling after finish rolling (the total time for laminar cooling was 15 seconds). Hence, it can be inferred that the temperature gradient yielded little influence on the microstructures and hardness along the thickness direction. The increase

in strength of Nb-HTi could be attributed to the higher hardening effect due to more Ti addition. A microstructural and precipitate analysis was performed to reveal the main reasons for the strength difference between these two samples.

B. Microstructures

The microstructures of the experimental steels at the 1/4-thickness position are displayed in Figure 3. Microstructures of both steels mainly consisted of micron-scale polygonal ferrite (PF) and granular bainite (GB) along with dispersive cementite particles. Large-sized PF grains were surrounded by smaller PF grains, and GB was mainly distributed along the grain boundaries of PF. Moreover, some tiny cementite particles were observed near PF boundaries. Generally, carbonitrides could not be detected in a low-magnification SEM image. It is important to note that the microstructures of both samples were mainly dominated by PF and the amount of GB was imperceptible. The concavo-convex morphology of PF occurred due to different orientations.^[38] It was found that in comparison to Nb-LTi steel, PF grains were apparently refined in Nb-HTi steel. More precipitations are the main reason for grain refinement in Nb-HTi steel with the same process. Precipitations aggregated on grain boundaries inhibited the growth of austenite grains and the microstructure was inherited in the ferrite grains. Further, low-temperature precipitations formed during subsequent cooling and coiling stages inhibited ferrite grain growth by pinning grain boundaries and, thus, contribute to ferrite grain refinement.

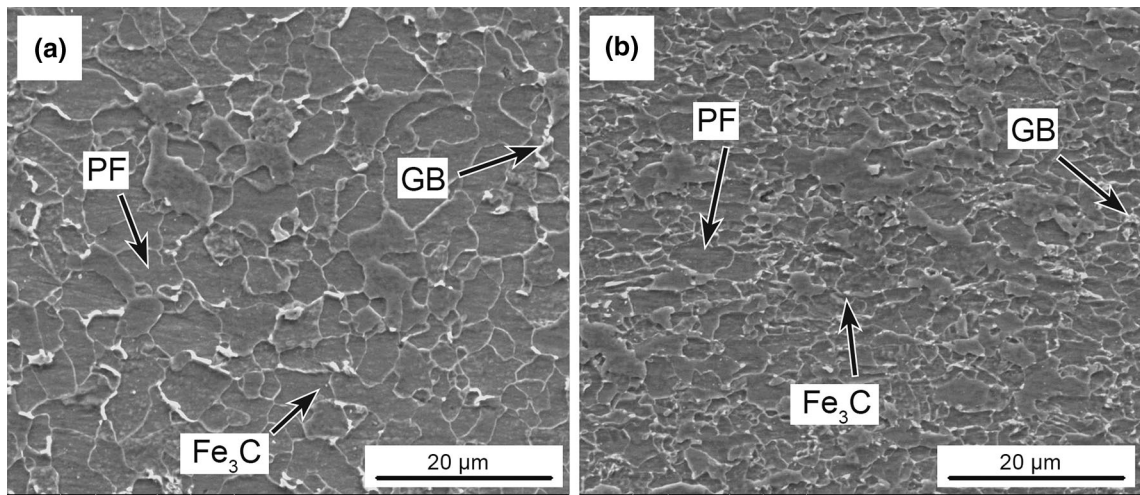


Fig. 3—Microstructures consisting of PF, GB, and cementite particles in (a) Nb-LTi and (b) Nb-HTi steels.

EBSD scans were performed in the cross section of the specimens to quantify mean crystallographic unit sizes. The approximate surface area of the microstructures was $10,000 \mu\text{m}^2$. Figure 4 displays the corresponding inverse pole figures (IPFs) and grain boundary maps (GBMs) of the tested steels. It is noticeable that ferrite grains had different orientations and ferrites with the orientation of $[101]\alpha$ were dominating in IPFs. In GBMs, high-angle grain boundaries (HAGBs; equal to or larger than 15 deg) are plotted in blue, whereas medium-low-angle grain boundaries ($4 \text{ to } 15 \text{ deg}$) are presented in red. Grain boundaries smaller than 4 deg were considered as sub-boundaries in the present study. It was found that PF was the predominant phase and formed HAGBs with relatively high densities. With an increase in Ti content, the length of HAGBs increased from 7.97 mm in Nb-LTi steel to 9.99 mm in Nb-HTi steel, thus signifying a grain refinement due to more Ti addition. In addition, in comparison to Nb-LTi steel, the fraction of HAGBs slightly increased in Nb-HTi steel.

The 4- and 15-deg misorientation crystallographic unit sizes were measured by EBSD based on mean equivalent diameter. The former misorientation criterion is an index of strength, whereas the unit size with respect to the 15 deg misorientation criterion is the main feature for controlling the cleavage fracture process (toughness).^[11] The total number of measured grains was high enough (about 200) to ensure the accuracy of the measurement. Figure 5 presents the unit size distributions and the accumulated area fractions of the specimens based on 4 and 15 deg misorientation criteria. The mean equivalent diameters for Nb-LTi and Nb-HTi steels were, respectively, measured as 3.5 and $2.8 \mu\text{m}$ based on 4 deg misorientation criterion, whereas when the 15 deg criterion was employed, the values were 4.6 and $3.5 \mu\text{m}$, respectively. This happened because medium-low-angle grain boundaries were not considered for the 15 deg criterion; thus, the influences of a small amount of bainites and ferrites were excluded.

However, ferrite grains were refined in Nb-HTi steel regardless of criteria.

Figure 6 illustrates a clear comparison of unit size distribution between Nb-LTi and Nb-HTi steels for 4 and 15 deg misorientation criteria. Accumulated grain area fractions were analyzed in order to confirm the refinement of ferrite grains in Nb-HTi steel. The curves of accumulated area fractions for both criteria moved toward the top left from Nb-LTi to Nb-HTi, thus confirming the formation of finer microstructures due to the addition of more Ti. This can be attributed to the relatively greater amount of Ti in the steel affecting both the parent austenite phase and the transformed ferrite phase by the Ti-alloyed carbides. In order to compare the microstructure homogeneity, a useful parameter (Dc10 pct) for evaluating the 10 pct length of the tail in the grain distribution is used to calculate a critical grain size for a fixed area fraction. In a grain size distribution histogram, Dc10 pct value refers to the cutoff grain size at 90 pct area fraction. D_{mean} is the average grain size of total grains. The ratio between Dc10 pct and D_{mean} ($\text{Dc10 pct}/D_{\text{mean}}$) represents the heterogeneity of grain distribution. Therefore, a lower ratio of $\text{Dc10 pct}/D_{\text{mean}}$ indicates a more homogeneous grain distribution.^[11] Detailed information on $\text{Dc10 pct}/D_{\text{mean}}$ is presented in the literature. Isasti *et al.*^[39] applied a similar method (Dc20 pct) in their work. In the present study, the values of $\text{Dc10 pct}/D_{\text{mean}}$ for Nb-LTi and Nb-HTi steels (based on 15 deg criterion) were found to be 3.91 and 3.43, respectively, thereby representing the formation of a more homogeneous ferrite microstructure in Nb-HTi steel. This can be attributed to the increased density of nucleation sites, which was high enough to achieve grain refinement in the entire unit size distribution in Nb-HTi steel. Similar results were also obtained for $\text{Dc10 pct}/D_{\text{mean}}$ by considering the 4 deg criterion.

Figure 7 manifests the relationship among the average yield strength, hardness, and mean unit size obtained from EBSD data for the tested criteria. The values of yield strength and hardness in Nb-HTi steel

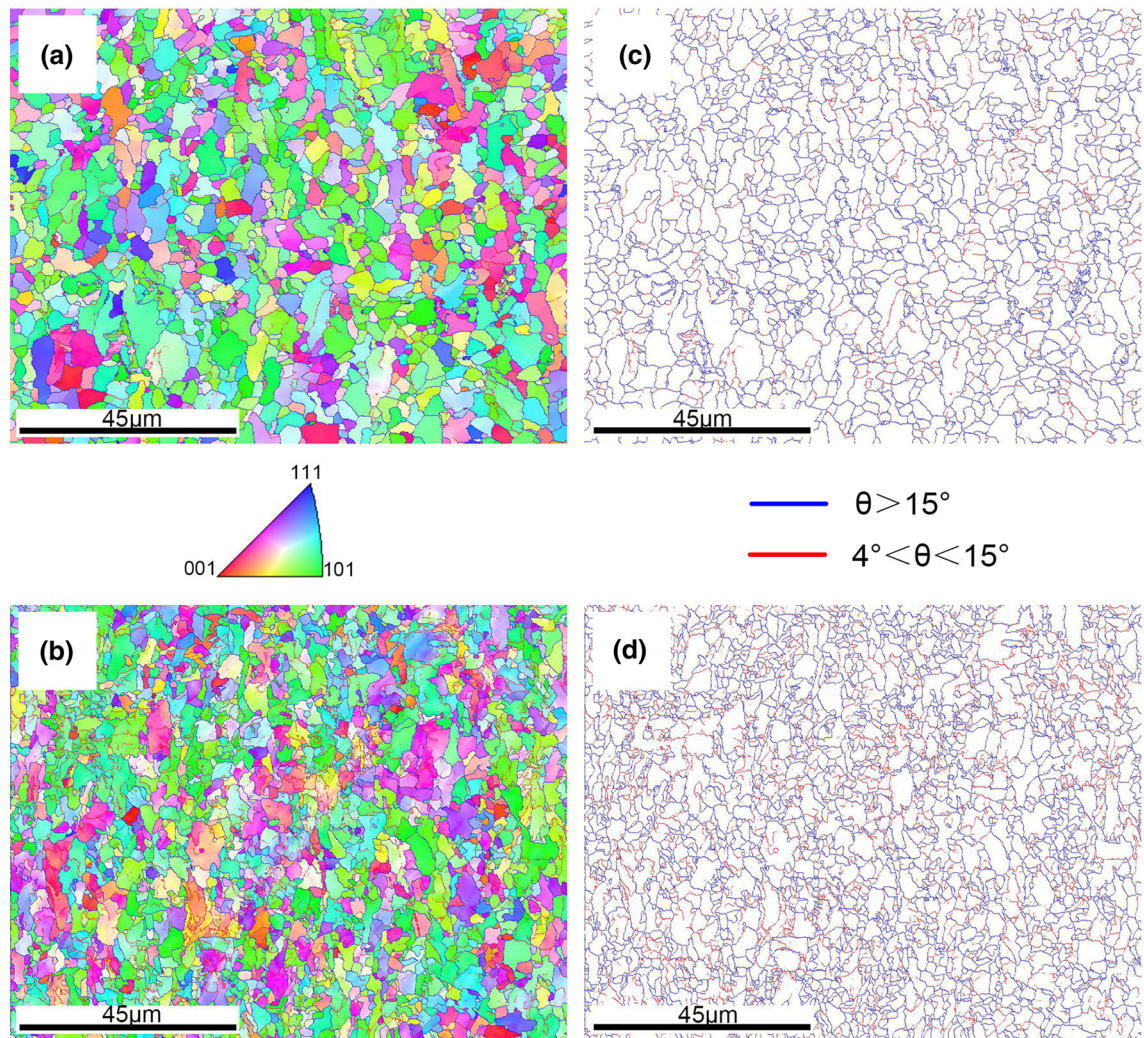


Fig. 4—EBSD microstructures of (a) and (c) Nb-LTi and (b) and (d) Nb-HTi steels: (a) and (b) IPF and (c) and (d) GBM (blue lines > 15 deg; red lines > 4 deg).

increased with a decrease in mean unit size and an increase in Ti content. The slope of the straight line represents the strength increment with respect to mean unit size. In comparison to the 15 deg criterion, a slightly larger increment (shown by the angle ω between the lines) was observed for the 4 deg criterion; thus, it can be attributed to the refined mean unit size in the 4 deg criterion.

C. Precipitations

TEM morphologies of precipitations and the corresponding representative EDS result of carbon replica samples are depicted in Figure 8. It is observable that the obtained morphologies were dominated by precipitations of spherical or torispherical (Nb, Ti)C particles. As the crystal structures of TiC and NbC are face-centered-cubic (as of the NaCl structure), the mutual dissolution occurred easily in these particles, thus making the precipitation of (Ti, Nb)C particles preferential. The presence of relatively larger (Nb, Ti)C particles can be inferred from the graphs. A large

amount of small (Nb, Ti)C particles, which were very hard to distinguish, formed a mosaic morphology (represented by the black rectangle in Figure 8(b)). However, these very small particles were observed in TEM micrographs at larger magnifications (Figure 8(c)). Moreover, these particles formed clusters and exhibited a cell-like or chain distribution, which indicates that precipitates mainly nucleated on dislocations. The size of large particles ranged between 15 and 100 nm, whereas the size of small cell-like particles did not exceed 15 nm. Moreover, it was roughly found that the volume fractions of both small- and large-sized (Nb, Ti)C particles in Nb-HTi steel were larger than those in Nb-LTi steel. Generally, precipitates formed in the γ phase presented a relatively larger dimension as compared to those generated in the low-temperature α phase. Previous studies have proved that carbides of several nanometers are the main cause of precipitation strengthening, whereas precipitates larger than 20 nm manifested relatively minor effects on strength.^[18]

Figure 9 displays the bright-field and dark-field images of large and small cell-like (Ti, Nb)C particles

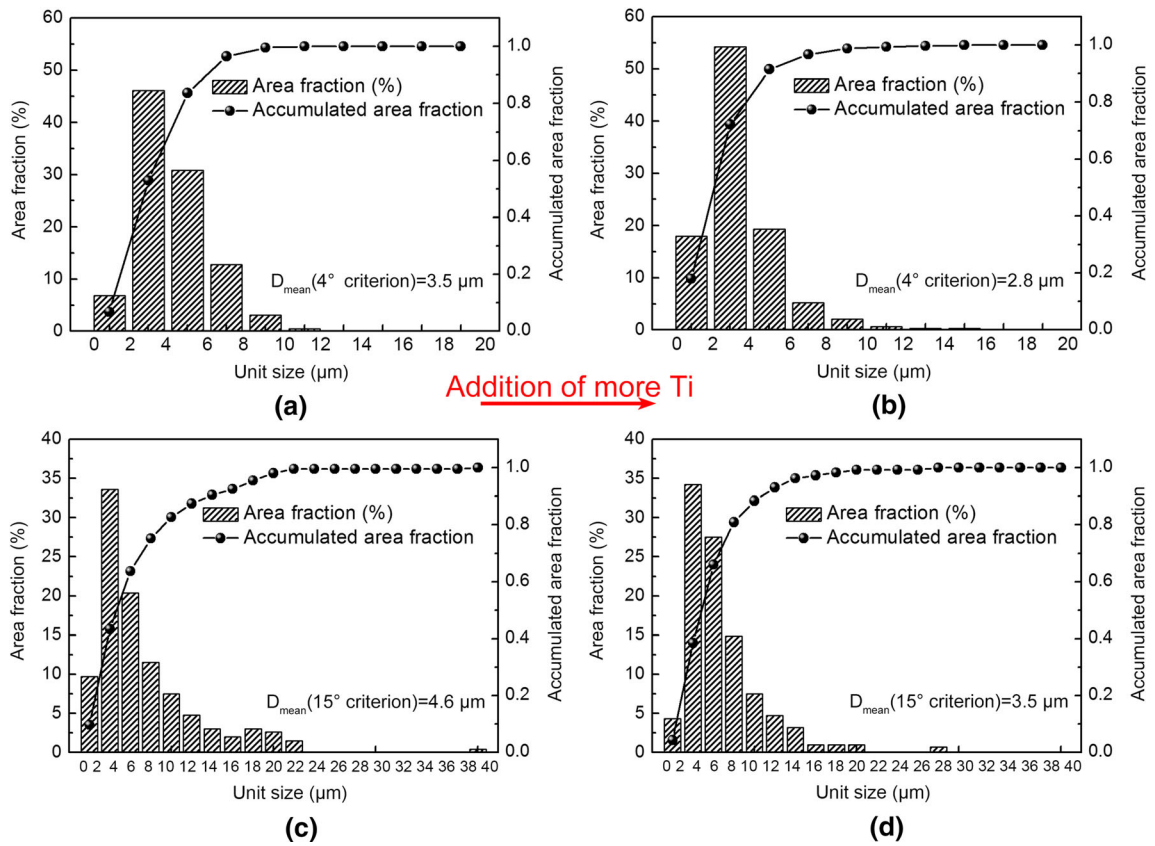


Fig. 5—Unit size distributions and accumulated area fractions for (a) and (c) Nb-LTi and (b) and (d) Nb-HTi steels using 4 and 15 deg misorientation criteria.

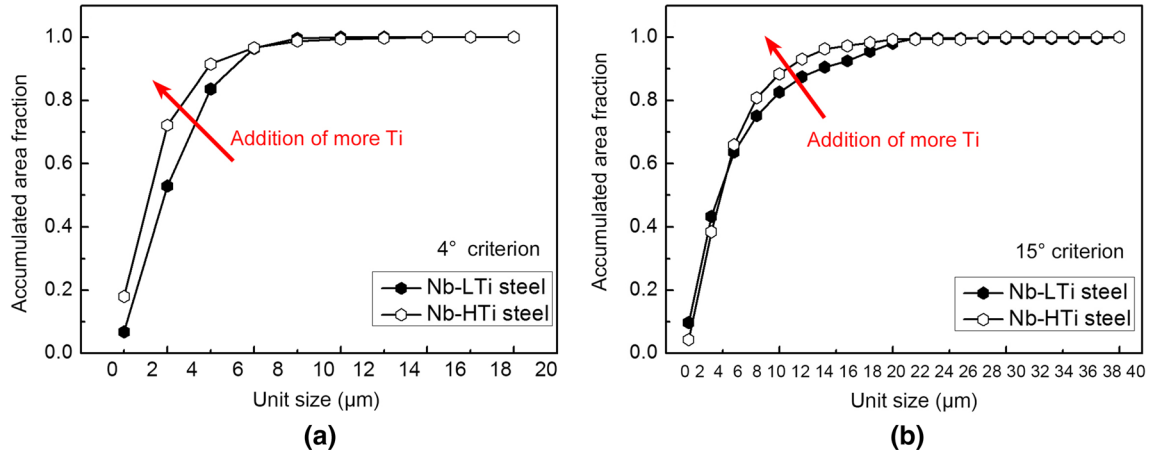


Fig. 6—Comparisons of unit size distributions in Nb-LTi and Nb-HTi steels using (a) 4 and (b) 15 deg criteria.

in Nb-HTi steel. Due to their small sizes, some nanoscale (Ti, Nb)C particles were hardly observed under dark-field conditions. The lattice constant of (Ti, Nb)C particles was measured as 0.435 nm based on the selected area diffraction pattern in Figure 9(c). Moreover, the known zone axes of [001] and [010] were also confirmed for both large and small (Ti, Nb)C particles. According to their diffraction patterns, the Kurdjumov–Sachs (KS) relationship with (111)(Ti, Nb)C//[110] α and $[10\bar{1}]$ (Ti, Nb)C//[$11\bar{1}$] α was obtained

for large (Ti, Nb)C particles and the Baker–Nutting (BN) relationship with (002)(Ti, Nb)C//(002) α and $[\bar{1}10]$ (Ti, Nb)C//[010] α was achieved for smaller ones. The KS relationship revealed that the large (Ti, Nb)C particles were strain-induced precipitations of γ at high temperatures. On the contrary, small cell-like (Ti, Nb)C particles were mainly formed after the cooling stage. Different precipitation temperatures resulted in different sizes of (Ti, Nb)C particles.

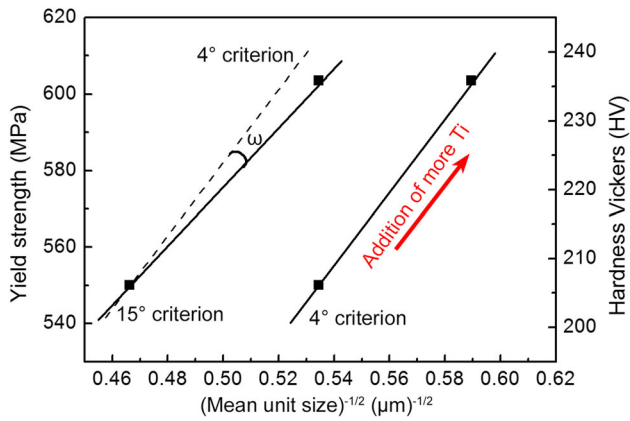


Fig. 7—Relationship between yield strength, hardness, and mean unit size for the tested criteria.

Figure 10 presents the size distribution of (Ti, Nb)C particles for carbon replica specimens of the experimental steels. Ten images of the same magnification were used to determine the average size of (Ti, Nb)C particles based on number density using JMATPRO software,^[40] and approximately 800 to 1000 particles were collected from each specimen to ensure a reliable analysis. The unimodal size distribution was observed for (Ti, Nb)C particles. Particles smaller than 20 nm were predominant and exceeded 80 pct of size distribution. Few overly large (Nb, Ti)C particles were also found because these nanoscale carbides with complex compositions manifested excellent thermal stability and maintained their tiny sizes even after the cooling process. Since the large particles (above 20 nm) hardly contribute to the strength, it would be better to exclude them for more accurate estimation of strength by the Ashby–Orowan

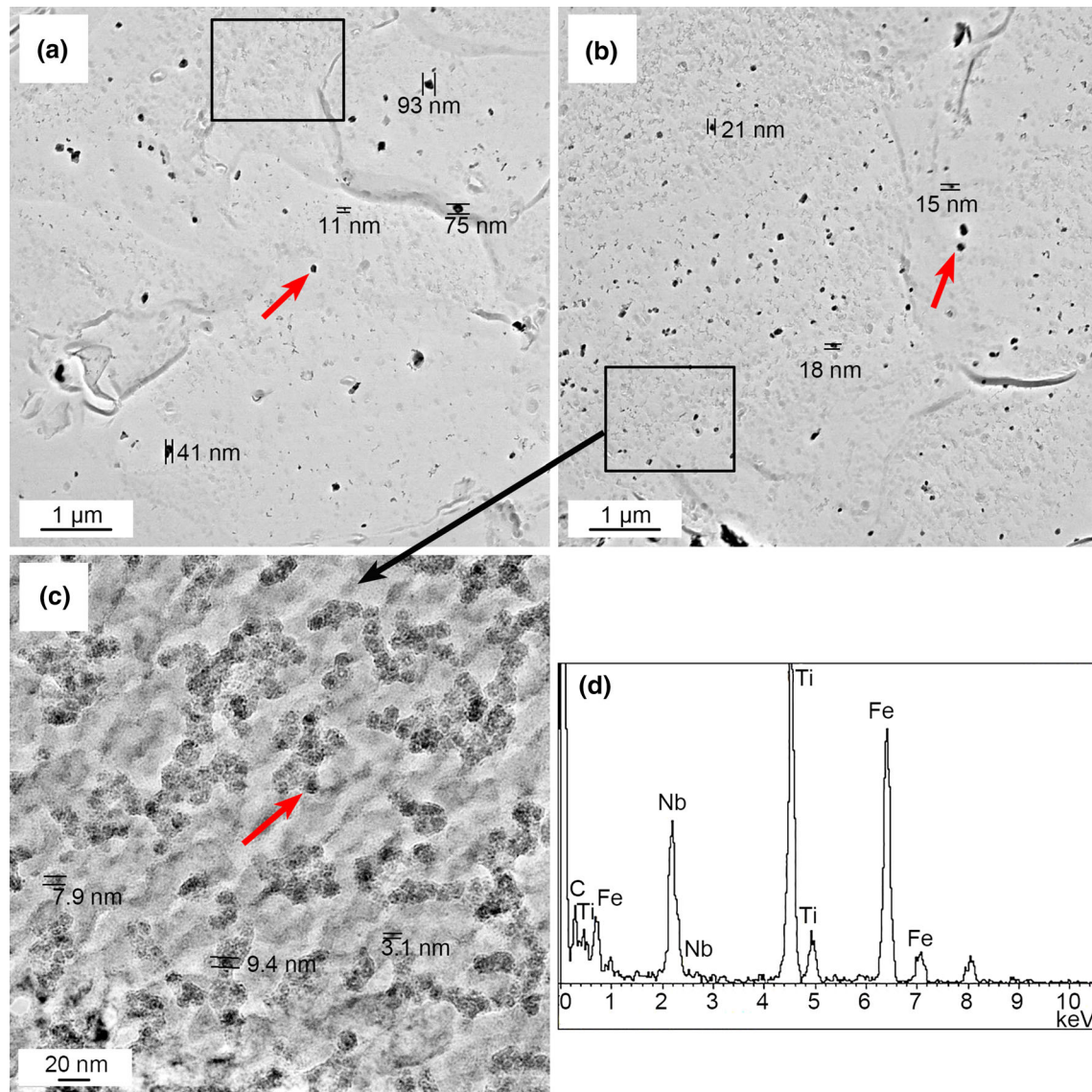


Fig. 8—TEM morphologies of precipitations in (a) Nb-LTi and (b) and (c) Nb-HTi steels. (d) Corresponding representative EDS result of (Nb, Ti)C particles from Nb-HTi steel.

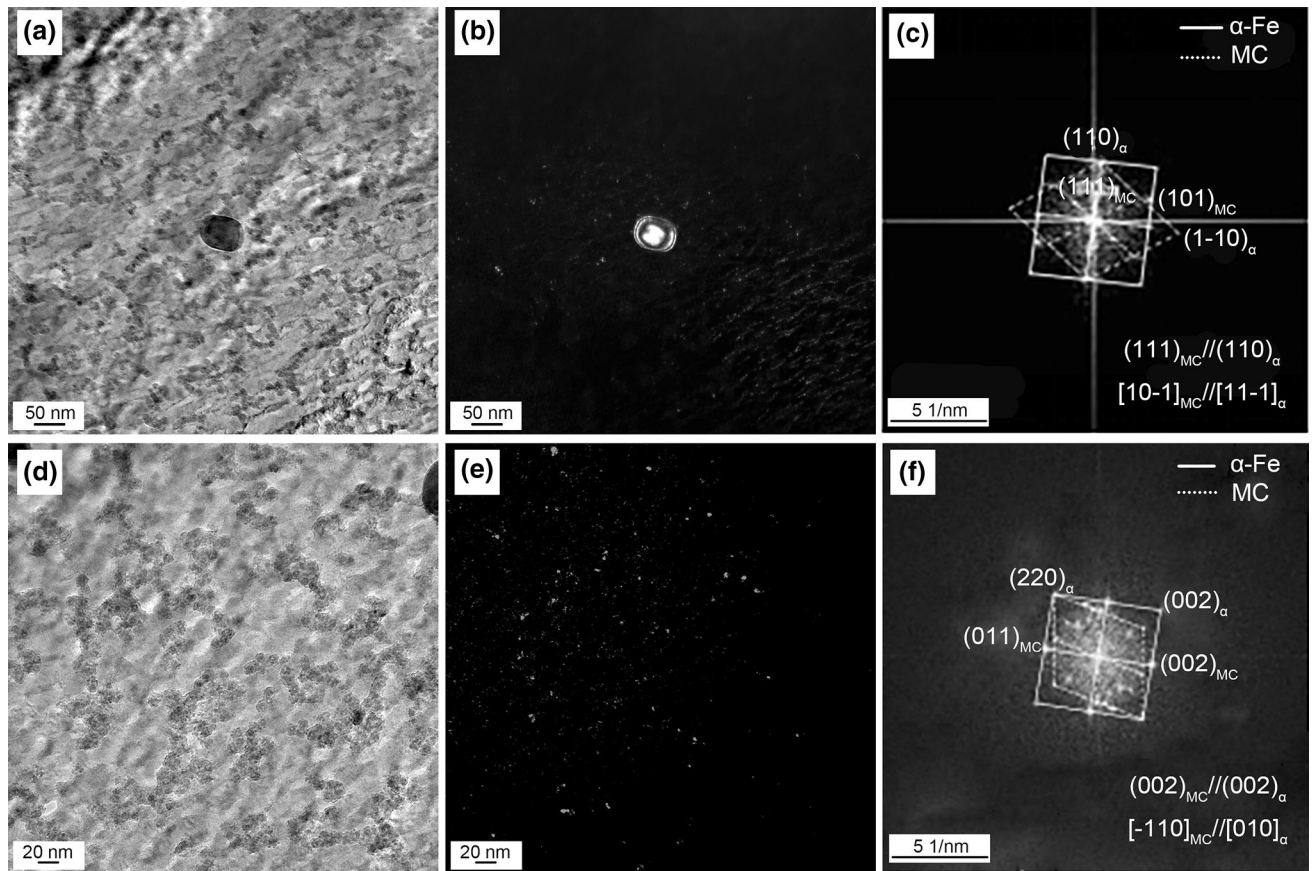


Fig. 9—Bright- and dark-field images and corresponding selected area diffraction patterns of (a) through (c) large and (d) through (f) small (Ti, Nb)C particles in Nb-HTi steel.

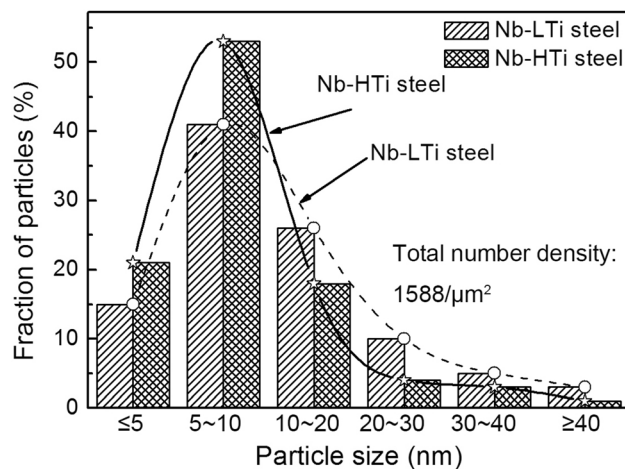


Fig. 10—Size distributions of (Ti, Nb)C particles for two steels.

equation.^[16,40] The mean diameters of the (Ti, Nb)C particles were measured as 13.3 and 10.5 nm by the mean linear intercept method. A large amount of particles were taken into consideration in the measurement to ensure the accuracy. Slightly refined (Ti, Nb)C particles in Nb-HTi steel could be ascribed to a relatively large fraction of (Nb, Ti)C particles with mosaic morphology.

Nitrogen preferentially precipitates in the form of large TiN particles at high temperatures and manifests little precipitation strength contribution in microalloyed steels. Moreover, these particles deteriorate the toughness of steels. In order to reveal the composition of cuboidal TiN particles, the three-dimensional structure of TiN was analyzed by FIB-SEM. Figure 11 exhibits the three-dimensional morphology of a TiN particle and the corresponding area and point scanning component analysis. The length and width of the rectangular TiN particle were measured as ~ 6.5 and ~ 3.8 μm , respectively. Unexpectedly, MnS particles of ~ 1.2 - μm diameter appeared on the TiN particle. This signifies that some small MnS particles acted as the heterogeneous nuclei for TiN formation.^[41] Ti only aggregates in the TiN precipitate and no enrichment of Ti is detected at other regions. This is because Ti has been consumed by the TiN precipitates and the relatively small (Ti, Nb)C particles.

Furthermore, it is evident from Figure 8 that Nb-HTi steel contained more small cell-like precipitates. For the replica technique, the volume from which particles were extracted was not exactly known. Therefore, the solid solubility product formula and the ideal stoichiometric ratio were used to precisely calculate the volume fraction of (Nb, Ti)C particles.^[17] As (Nb, Ti)C particles form a continuous solid solution, $\text{Nb}_x\text{Ti}_y\text{C}$ can be used to

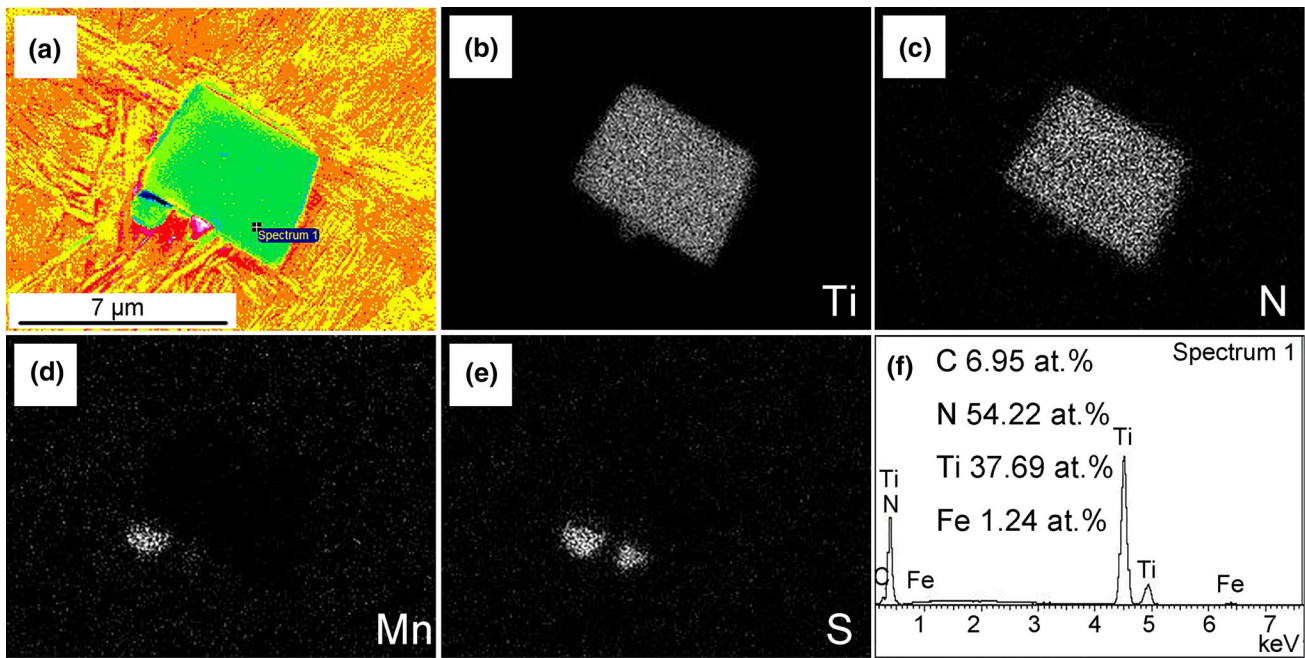


Fig. 11—(a) Three-dimensional morphology of a TiN particle and (b) through (e) corresponding area and (f) point scanning component analysis.

represent the chemical formula of (Nb, Ti)C with $x + y = 1$. According to the literature,^[4-6,17-19] the solutions of NbC and TiC in the γ and α phases can be expressed by Eqs. [1] through [4]:

$$\lg\{[\text{Nb}][\text{C}]\}_{\gamma} = 2.96 - 7510/T \quad [1]$$

$$\lg\{[\text{Ti}][\text{C}]\}_{\gamma} = 2.75 - 7000/T \quad [2]$$

$$\lg\{[\text{Nb}][\text{C}]\}_{\alpha} = 3.9 - 9930/T \quad [3]$$

$$\lg\{[\text{Ti}][\text{C}]\}_{\alpha} = 4.4 - 9575/T \quad [4]$$

where [M] (M = Nb, Ti, C) is the solid solution amount of element M in the γ and α phases (subscripts γ and α represent the solid solution formulas for austenites and ferrites, respectively) and T is the solid solution temperature. The value of [Ti] in the γ phase was determined as the difference between the original amount of Ti and the consumed amount of TiN when N fully precipitated as TiN at high temperatures. The initial amounts of other elements were their equilibrium solution contents at 1230 °C. The equilibrium solution contents of the elements at 880 °C were regarded as their initial amounts in the α phase. The ideal stoichiometric ratios of NbC and TiC were 7.735 and 3.991, respectively. Therefore,

$$\frac{\text{Nb} - [\text{Nb}]}{(\text{C} - [\text{C}])x} = 7.735 \quad [5]$$

$$\frac{\text{Ti} - [\text{Ti}]}{(\text{C} - [\text{C}])y} = 3.991 \quad [6]$$

The volume fraction (f_v) of the precipitated second phase was calculated by Eq. [7]:

$$f_v = (M - [M]) \frac{\rho_{\text{Fe}}}{100\rho_{\text{MC}}} \quad [7]$$

where M (M = Nb, Ti, C) is the weight percentage of different elements; $M - [M]$ represents precipitates in the equilibrium state; and ρ_{Fe} and ρ_{MC} are the densities of Fe and precipitates, respectively. The linear interpolation method (Eq. [8]) was employed to obtain the value of ρ_{MC} :

$$\rho_{\text{MC}} = k_1\rho_{\text{M}_1\text{C}} + k_2\rho_{\text{M}_2\text{C}} \quad [8]$$

where k_1 and k_2 are the proportions of M_1C and M_2C phases in the MC phase. Moreover, $k_1 + k_2 = 1$ and the values of ρ_{NbC} and ρ_{TiC} were 7.803×10^3 and 4.944×10^3 kg/m³, respectively. Based on the aforementioned formula, the volume fractions of (Nb, Ti)C particles in Nb-LTi and Nb-HTi steels were calculated as 0.084 and 0.145 pct, respectively, and these results are in good agreement with the morphology presented in Figure 8. Therefore, an increase in Ti content caused an increase in the volume fraction of (Nb, Ti)C particles. It happened because nucleation is a type of diffusion transformation and depends on the diffusion of C, Ti, and Nb atoms. The atomic diffusion is generally found in a positive correlation with temperature and atom contents. Under the same thermal cycle, the volume fraction of precipitates started to increase with the increasing alloying content. At a low alloy level, the precipitation behavior is likely to be limited. In addition, with the increased volume fraction and the decreased size of (Nb, Ti)C particles, the pinning effect became

dominant in the α phase and restricted the growth of ferrite grains.

D. Estimation of Strength

The yield strength (σ_y) of low-carbon microalloyed steels can be expressed as a combination of different strengthening mechanisms, such as solid solution (σ_{ss}), grain size (σ_g), dislocation density (σ_ρ), and fine precipitation (σ_{ppt}).^[4-6,17-19] For some microalloyed steels, due to the lack of an accurate measurement of precipitate volume fraction, the contribution of fine precipitation (σ_{ppt}) is estimated by subtracting the strengthening associated with lattice friction, grain size, solute, and dislocation from the experimental yield strength value.^[40] In the present study, the individual contribution of each strengthening mechanism was estimated by different approaches reported in previous literature.^[4-6] The strengthening contribution for the experimental steels can be expressed by Eq. [9]:

$$\sigma_y = \sigma_o + \sigma_{ss} + \sigma_g + \sigma_\rho + \sigma_{ppt} \quad [9]$$

where σ_o represents the crystal lattice strengthening (in the present study, the value of σ_o was assumed to be 48 MPa^[17]). The solid solution strengthening (σ_{ss}) was evaluated by Eq. [10]:^[17-19]

$$\begin{aligned} \sigma_{ss} = & 4570[C] + 3750[N] + 37[Mn] + 83[Si] + 470[P] \\ & + 2.9[V] + 80[Ti + Nb] + 11[Mo] - 30[Cr] \end{aligned} \quad [10]$$

where $[M]$ ($M = C, N, Mn, \dots$) is the mass fraction of element X in the α phase. It is generally considered that Si, Mn, Cr, and P are in full dissolution. The value of $[N]$ was equal to 0 due to the adequate precipitation of TiN particles and very low content of nitrogen. In addition, the value of $[C]$ was selected as 0.0218 wt pct due to the maximum solution amount of C in ferrite at the coiling temperature of 630 °C according to the equilibrium Fe-C phase diagram. The maximum solution amount of C in ferrite would decrease at a lower coiling temperature. However, the solution amount of C remained unchanged because the C would not precipitate during air cooling. Thus, the solid solutions (σ_{ss}) of Nb-LTi and Nb-HTi steels were estimated as 152.2 and 150.6 MPa, respectively. The slight change in solid solution strengthening was considered to be reasonable due to the small variation in solid solution content of elements in the steels.

The grain refinement strengthening (σ_g) was evaluated by the Hall–Petch relationship (Eq. [11]):

$$\sigma_g = kd^{-\frac{1}{2}} \quad [11]$$

where k is a constant (MPa m^{0.5}) and d is the average size of ferrite grains (meters). The value of k for high-strength low-alloyed steels is equal to 0.55 MPa m^{0.5}.^[17] Grain size calculated by the 15 deg misorientation criterion was used for the evaluation of refinement strengthening. The grain refinement strengthening values for Nb-LTi and Nb-HTi steels were estimated as 256.4 and 294.1 MPa, respectively.

Figure 12 manifests high-magnification ferrite grain images for thin foil specimens. A large amount of dislocations were observed, and small cell-like (Ti, Nb)C particles were interlaced with dislocation lines (shown by red arrows). The strain hardening region in the plastic part of Figure 2 may be caused by the pileup of dislocations due to the appearance of (Ti, Nb)C particles. Dislocation lines acted as fast diffusion channels and facilitated the formation of rich-solution cores. Cahn^[42] propounded the theory of nucleation on dislocation lines by assuming that the new nucleus embryo was formed along dislocation lines and the section of the nucleus embryo perpendicular to dislocation lines was a circle. If the diameter of the circle is d , the free energy increment (ΔG_{fe}) can be expressed by Eq. [12]:

$$\Delta G_{fe} = \frac{1}{4}\pi d^2 \Delta G_{vfe} + \pi d\sigma - A \ln d + C \quad [12]$$

where C is a constant irrelevant to d ; σ is the surface energy per unit area; ΔG_{vfe} is the increment in volume free energy; A is the superficial area of the nucleus embryo and is equal to $G\mathbf{b}^2/[4\pi(1-\nu)]$ or $G\mathbf{b}^2/(4\pi)$ for edge or screw dislocations, respectively; G is the shear modulus of elasticity; ν is the Poisson ratio; and \mathbf{b} is the dislocation Burgers vector. The critical core size (d_d^*) of the nucleus embryo was calculated by Eq. [13]:

$$d_d^* = -\frac{\sigma}{\Delta G_{vfe}} \left[1 \pm (1 + \alpha)^{1/2} \right] \quad [13]$$

where α is an index and equals $2A\Delta G_{vfe}/\pi\sigma^2$. When $\alpha < -1$, the nucleus embryo was formed along dislocation lines without thermal activation. Yong^[19] posited the theory of nucleation on dislocation lines and reported that the nucleation on dislocation lines was spontaneous due to the decrease in free energy during phase transformation. The corresponding nucleation rate (I_d) can be calculated by Eq. [14]:

$$\begin{aligned} I_d = & n_V \alpha_d^* \rho \nu \cdot \pi \rho \mathbf{b}^2 \exp\left(-\frac{Q_d}{kT}\right) \exp\left(-\frac{(1+\beta)^{\frac{3}{2}} \Delta G^*}{kT}\right) \\ = & \pi \rho \mathbf{b}^2 \frac{d_d^{*2}}{d^{*2}} \exp\left(\frac{Q - Q_d}{kT}\right) \exp\left\{\frac{\left[1 - (1 + \beta)^{3/2}\right] \Delta G^*}{kT}\right\} \\ & \cdot I \end{aligned} \quad [14]$$

where Q and Q_d are the intracrystalline diffusion activation energy and the grain boundary diffusion activation energy, respectively; ρ is the dislocation density; and $2b$ is the diameter of the dislocation pipeline core. The term β represents the condition of extracting a root from the equation, and the real roots are obtained if $(1 + \beta) \geq 1$. Only significant parameters are pointed out and other parameters can be found in the works of Cahn^[42] and Yong.^[19] According to Eq. [14], it can be inferred that the higher dislocation density expedited the nucleation of the second phase, such as (Ti, Nb)C particles, along dislocation lines.

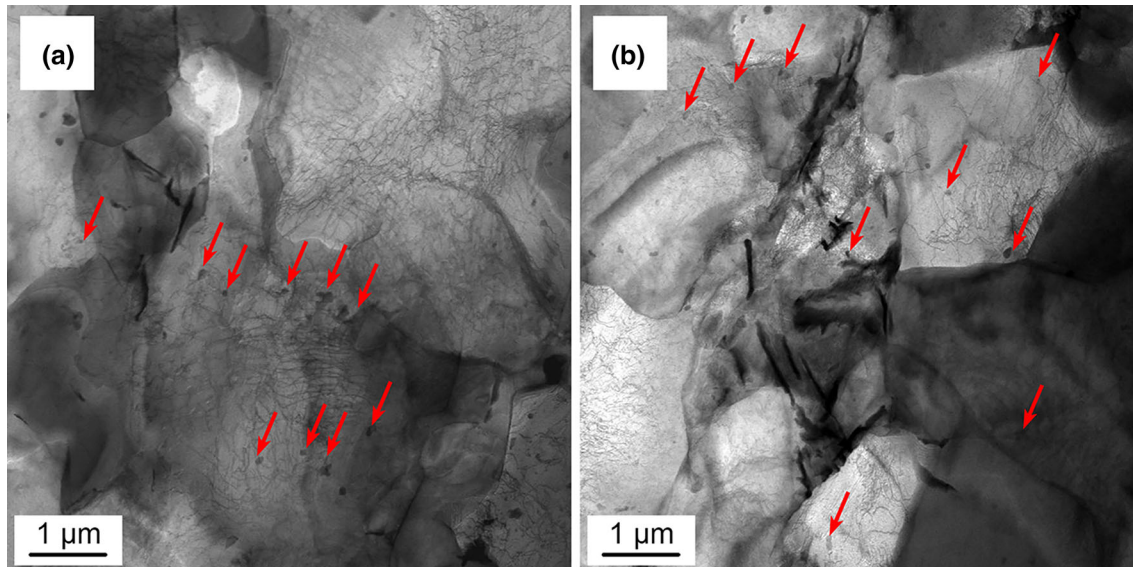


Fig. 12—High-magnification TEM images of ferrite grains in (a) Nb-LTi and (b) Nb-HTi steels.

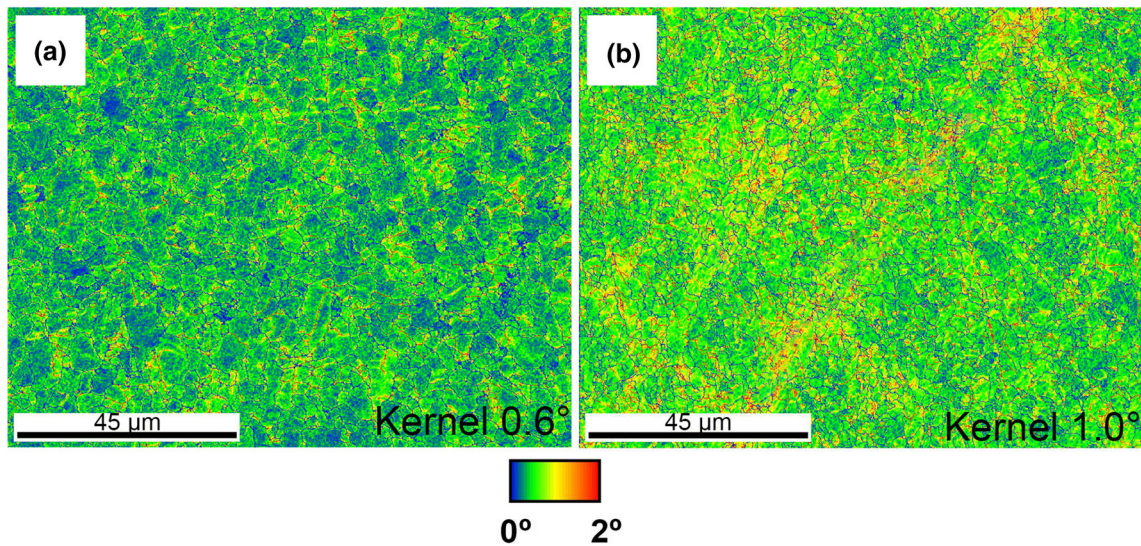


Fig. 13—Kernel average misorientation elucidating the dislocation densities for (a) Nb-LTi and (b) Nb-HTi steels.

Moreover, from the results of carbon replicas in Figure 8, it can be deduced that a large amount of small (Ti, Nb)C particles were formed in Nb-HTi steel by relatively large dislocation density. The high dislocation density occurred due to the increasing high-temperature Ti-precipitation pinning of the dislocations by greater Ti addition.

Generally, dislocation hardening is estimated by a reference dislocation density in low-carbon ferrite steels. In order to quantify the dislocation density (ρ), the kernel average misorientation (θ) in Figure 13 was determined by the first neighbor criterion. The values of θ for Nb-LTi and Nb-HTi steel were estimated as 0.6 and 1, respectively. Similar results for kernel average misorientation in microalloyed steels are also reported

in the literature.^[11] Equation [15] presents the relationship between kernel average misorientation and dislocation density in per unit area:^[43]

$$\rho = \alpha\theta/ub \quad [15]$$

where u is the unit length, \mathbf{b} is the Burgers vector of magnitude 2.5×10^{-10} m, and α equals 2 or 4 for a pure tilt grain boundary or a pure twist boundary, respectively. In the present work, the value of α was considered as 2. It should be noted that only geometrically necessary dislocations (GNDs) were considered in the EBSD analysis because GNDs can accommodate the lattice curvature and develop nonuniform strains in the crystal. On the contrary, statistically stored dislocations (SSDs) cannot accumulatively affect the

crystal lattice curvature. These two types of dislocation can be distinguished by spatial resolution and the measurement accuracy of orientation. The Taylor equation (Eq. [16]) was employed to determine dislocation strengthening (σ_ρ) according to the measured dislocation density.^[19]

$$\sigma_\rho = \alpha M G b \rho^{1/2} \quad [16]$$

where α is equal to 0.38, M represents the Taylor factor and equals 2.2 for ferritic grains, G is the shear modulus (81,600 MPa for steels), and b is the Burgers vector of magnitude 2.5×10^{-10} m. By combining Eqs. [15] and [16], the dislocation strengthening values for Nb-LTi and Nb-HTi steels were estimated as 61 and 71 MPa, respectively, confirming the increase in the volume fraction of (Ti, Nb)C particles along dislocation lines in Nb-HTi steel.

Now, assuming the random dispersion of precipitates on a slip plane, the precipitation strengthening (σ_{ppt}) was evaluated by the Ashby–Orowan formula based on the average size of (Ti, Nb)C particles and corresponding volume fraction:

$$\sigma_{ppt} = 8.995 \times 10^3 \frac{f_v^{1/2}}{d_p} \ln(2.417 d_p) \quad [17]$$

where f_v is the volume fraction of precipitates (pct) and d_p is the average size of precipitates (nm). It should be noted that the Ashby–Orowan equation is valid only for bypassing precipitate–dislocation interactions. It is impossible for a (Ti, Nb)C particle to be sheared as its extreme dimension is larger than the critical dimension for a shearable mechanism. The precipitation strengthening values for Nb-LTi and Nb-HTi steels were calculated as 77.9 and 120.3 MPa, respectively. Due to a relatively smaller size and larger volume fraction of (Ti, Nb)C particles in Nb-HTi steel, the precipitation strengthening was enhanced by 42.4 MPa. Nitride precipitations, such as TiN, were not considered in the calculation because the nitrogen content in the steel was extremely small as the vacuum treatment is generally

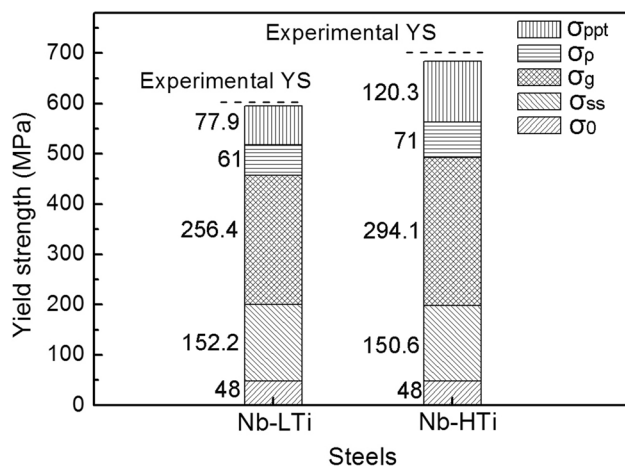


Fig. 14—Strengthening contributions of different strengthening mechanisms.

applied during the steelmaking process to ensure the purity of the molten steel.

Figure 14 summarizes the strengthening contributions of different strengthening mechanisms. Although the calculated yield strengths (σ_y) of the experimental steels were slightly lower than the experimental values, the obtained results manifested good consistency with the measured values. Calculation errors mainly came from statistical errors in the size of ferrite grains and (Ti, Nb)C particles. In addition, SSDs were not considered in the calculation of dislocation strengthening. Therefore, it can be deduced from Figure 14 that the difference in yield strength between two steel specimens mainly occurred from grain refinement strengthening and precipitation strengthening. Moreover, grain refinement strengthening and precipitation strengthening also contributed to the increase in yield strength of Nb-HTi steel because the increase in Ti content of Nb-HTi steel resulted in more finer grains and precipitates.

IV. CONCLUSIONS

The microstructural characterization and tensile tests were systematically performed for two Nb-Ti microalloyed steels with different Ti contents. The quantitative analysis of strength contribution was carried out based on different mechanisms. The main inferences are presented as follows.

1. Grain refinement strengthening, precipitation strengthening, and dislocation strengthening were responsible for the enhanced mechanical properties of the steel with high Ti content (the first two strengthening contributions were found to be more prominent).
2. Ferrite grains were refined due to the addition of more Ti regardless of the 4 and 15 deg criteria. A large amount of Ti formed more precipitates and affected both the parent austenite phase and the transformed ferrite phase. In addition, the increase in Ti content resulted in a more homogeneous ferrite microstructure.
3. The KS (for larger (Ti, Nb)C particles) and the BN (for smaller cell-like (Ti, Nb)C particles) relationships indicate that a large amount of nanoscale (Ti, Nb)C particles precipitated after the coiling stage.
4. The formation of more high-temperature Ti precipitations led to a higher dislocation density and accelerated the nucleation of (Ti, Nb)C particles along the dislocation lines.

ACKNOWLEDGMENTS

The authors gratefully acknowledge the financial support from The National Natural Science Foundation of China (NSFC) (Grant No. 51874216), The Major Projects of Technology Innovation of Hubei Province (Grant No. 2017AAA116), the Hebei Joint

REFERENCES

1. M. Ghosh, K. Bart, S.K. Das, B.R. Kumar, A.K. Pramanick, J. Chakraborty, G. Das, S. Hadas, S. Bharathy, and S.K. Ray: *Metall. Mater. Trans. A*, 2014, vol. 45A, pp. 2719–31.
2. Y.W. Kim, S.W. Song, S.J. Seo, S.G. Hong, and C.S. Lee: *Mater. Sci. Eng. A*, 2013, vol. 565, pp. 430–38.
3. X. Mao, X. Huo, X. Sun, and Y. Chai: *Mater. Process. Technol.*, 2010, vol. 210, pp. 1660–66.
4. G.S. Leire, L. Beatriz, and P. Beatriz: *Mater. Sci. Eng. A*, 2019, vol. 748, pp. 386–95.
5. A. Iza-Mendia, M.A. Altuna, B. Pereda, and I. Gutierrez: *Metall. Mater. Trans. A*, 2012, vol. 43A, pp. 4553–70.
6. N. Isasti, D. Jorge-Badiola, M.L. Taheri, and P. Uranga: *Metall. Mater. Int.*, 2014, vol. 20, pp. 807–17.
7. S.F. Medina, M. Chapa, P. Valles, A. Quispe, and M.I. Vega: *ISIJ Int.*, 1999, vol. 39, pp. 930–36.
8. R. Lagneborg, T. Siwecki, S. Zajac, and B. Hutchinson: *Scand. J. Metall.*, 1999, vol. 28, pp. 186–241.
9. S. Freeman and R.W.K. Honeycombe: *Met. Sci.*, 1977, vol. 11, pp. 59–64.
10. R. Uemori, R. Chijiwa, H. Tamehiro, and H. Morikawa: *Appl. Surf. Sci.*, 1994, vols. 76–77, pp. 255–60.
11. N. Isasti, D. Jorge-Badiola, M.L. Taheri, L. Beatriz, and P. Uranga: *Metall. Mater. Trans. A*, 2011, vol. 42A, pp. 3729–42.
12. X.P. Mao: *Microalloying Technology on Thin Slab Casting and Direct Rolling Process*, Metal Industry Press, Beijing, 2008.
13. N. Isasti, D. Jorge-Badiola, M.L. Taheri, and P. Uranga: *Metall. Mater. Trans. A*, 2014, vol. 45A, pp. 4960–71.
14. R.D.K. Misra, H. Nathani, J.E. Hartmann, and F. Siciliano: *Mater. Sci. Eng. A*, 2005, vol. 394, pp. 339–52.
15. G. Xu, X.L. Gan, G.J. Ma, F. Luo, and H. Zou: *Mater. Des.*, 2010, vol. 31, pp. 2891–96.
16. T. Gladman: *Met. Sci. J.*, 1999, vol. 15, pp. 30–36.
17. H.H. Huang, G.W. Yang, G. Zhao, X.P. Mao, X.L. Gan, Q.L. Yin, and H. Yi: *Mater. Sci. Eng. A*, 2018, vol. 736, pp. 148–55.
18. K. Zhang, Z.D. Li, X.J. Sun, Q.L. Yong, J.W. Yang, Y.M. Li, and P.L. Zhao: *Acta Metall. Sin. (Eng. Lett.)*, 2015, vol. 28, pp. 641–48.
19. Q.L. Yong: *Microalloyed Steels Physical and Mechanical Metallurgy*, China Machine Press, Beijing, 1989.
20. C. Ioannidou, Z. Arechabaleta, A. Navarro-López, A. Rijkenberg, R.M. Dalgliesh, S. Kölling, V. Bliznuk, C. Pappas, J. Sietsma, A.A. van Well, and S. Erik Offerman: *Acta Mater.*, 2019, vol. 181, pp. 10–24.
21. Y.W. Kim, J.H. Kim, S.G. Hong, and C.S. Lee: *Mater. Sci. Eng. A*, 2014, vol. 605, pp. 244–52.
22. G.W. Yang, X.J. Sun, Q.L. Yong, Z.D. Li, and X.X. Li: *IronSteel Res. Int.*, 2014, vol. 21, pp. 757–64.
23. G.W. Yang, X.J. Sun, Z.D. Li, X.X. Li, and Q.L. Yong: *Mater. Des.*, 2013, vol. 50, pp. 102–07.
24. H.W. Yen, P.Y. Chen, C.Y. Huang, and J.R. Yang: *Acta Mater.*, 2011, vol. 59, pp. 6264–74.
25. Y.F. Shen, C.M. Wang, and X. Sun: *Mater. Sci. Eng. A*, 2011, vol. 528, pp. 8150–56.
26. H.L. Yang, G. Xu, L. Wang, Q. Yuan, and B. He: *Met. Sci. Heat Treat.*, 2017, vol. 1, pp. 7–12.
27. C.P. Reip, S. Shanmugam, and R.D.K. Misra: *Mater. Sci. Eng. A*, 2006, vol. 424, pp. 307–17.
28. Z. Jia, R.D.K. Misra, R.O. Malley, and S.J. Jansto: *Mater. Sci. Eng. A*, 2011, vol. 528, pp. 7077–83.
29. M.D. Mulholland and D.N. Seidman: *Acta Mater.*, 2011, vol. 59, pp. 1881–97.
30. H.L. Yi, Z.Y. Liu, G.D. Wang, and D. Wu: *IronSteel Res. Int.*, 2010, vol. 17, pp. 54–64.
31. Q. Liu, H. Peter, H.W. Zhang, Q. Wang, P. Jonsson, and K. Nakajima: *ISIJ Int.*, 2012, vol. 52, pp. 2288–94.
32. X.L. Gan, G. Xu, G. Zhao, M.X. Zhou, and Z. Cai: *J. Wuhan Univ. Technol. (Mater. Sci. Ed.)*, 2018, vol. 5, pp. 1193–97.
33. M. Zhu, G. Xu, M.X. Zhou, and H.J. Hu: *J. Wuhan Univ. Technol. (Mater. Sci. Ed.)*, 2019, vol. 3, pp. 692–97.
34. S.Q. Yuan and G.L. Liang: *Mater. Lett.*, 2009, vol. 27, pp. 2324–26.
35. R.Z. Wang, C.I. Garcia, M. Hua, K. Cho, H.T. Zhang, and A.J. Deardo: *ISIJ Int.*, 2006, vol. 9, pp. 1345–53.
36. K. Zhang, Z.D. Li, F.L. Sui, Z.H. Zhu, X.F. Zhang, X.J. Sun, Z.Y. Huang, and Q.L. Yong: *Acta Metall. Sin.*, 2018, vol. 1, pp. 32–38.
37. P.K. Patra, S. Sam, M. Singhai, S.S. Hazra, G.D.J. Ram, and S.R. Bakshi: *Trans. Ind. Inst. Met.*, 2017, vol. 70, pp. 1773–81.
38. Q. Yuan, G. Xu, M. Liu, S. Liu, and H.J. Hu: *Trans. Ind. Inst. Met.*, 2019, vol. 72, pp. 741–49.
39. N. Isasti, J.B. Denis, M.L. Taheri, and P. Uranga: *Metall. Mater. Trans. A*, 2013, vol. 44A, pp. 3552–63.
40. A. Rijkenberg, A. Blowey, P. Bellina, and C. Wooffindin: *4th Int. Conf. on Steels in Cars and Trucks*, Braunschweig, Germany, 2014, pp. 15–19.
41. J.W. Fu, Q.Q. Nie, W.X. Qiu, J.Q. Liu, and Y.C. Wu: *Mater. Charact.*, 2017, vol. 133, pp. 176–84.
42. J.W. Cahn: *Acta Metall.*, 1957, vol. 5, pp. 168–72.
43. H.W. Yen, C.Y. Chen, T.Y. Wang, C.Y. Huang, and J.R. Yang: *Mater. Sci. Technol.*, 2013, vol. 26, pp. 421–30.

Publisher's Note Springer Nature remains neutral with regard to jurisdictional claims in published maps and institutional affiliations.